Full-Order Terminal Sliding Mode Observer With Adaptive Gain Based Sensorless Control for Linear Induction Machine in Urban Rail Transit

Siwei Cheng, Wei Xu, *Fellow, IEEE*, Jian Ge, *Member, IEEE*, Yirong Tang, Han Xiao, Zhongyong Chen, and Ion Boldea, *Life Fellow, IEEE*

***Abstract*—Speed sensorless control is essential for linear induction machines (LIMs) in urban rail transit. However, it is difficult to obtain the accurate speed when the mutual inductance of LIM is changed nonlinearly due to the end effect, especially in high-speed flux-weakening region. To enhance the robustness of the sensorless control system against such parameter changes, an improved speed sensorless control based on full-order terminal sliding mode (FOTSM) observer with adaptive gain is proposed in this article. First, to implement the minimum use of parameters affected by end effect, an active flux observer with improved FOTSM is constructed in the back electromotive force-primary current model. Then, an adaptive gain is designed to guarantee the stability and effectively attenuate the chattering. After acquiring the accurate estimated active flux, a novel speed observer based FOTSM is established, where the mutual inductance and estimated active flux are decoupled. Finally, comprehensive simulation and experimental results have demonstrated the effectiveness and feasibility of the proposed method.**

***Index Terms*—Flux weakening (FW), linear induction machine (LIM), sensorless control, sliding mode observer (SMO).**

Received 12 August 2025; revised 20 November 2025 and 5 January 2026; accepted 7 January 2026. Date of publication 12 January 2026; date of current version 20 March 2026. This work was supported in part by the Strategic Priority Research Program of Chinese Academy of Sciences under Grant E5XB1330, in part by the National Natural Science Foundation of China under Grant 52277050 and Grant 52407050, in part by the High-level Talent Program at Chinese Academy of Sciences under Grant E42K0801, in part by the Science and Technology Research Foundation of Institute of Electrical Engineering of Chinese Academy of Sciences under Grant IEERF250307, and in part by Shenzhen Fundamental Research Project (General Program) under Grant JCYJ20230807143701003. Recommended for publication by Associate Editor A. J. Marques Cardoso. *(Corresponding author: Wei Xu.)*

Siwei Cheng, Jian Ge, Han Xiao, and Zhongyong Chen are with the State Key Laboratory of High-Density Electrical Energy Conversion, School of Electrical and Electronic Engineering, Huazhong University of Science and Technology, Wuhan 430074, China (e-mail: siweicheng@hust.edu.cn; gejian1994@hust.edu.cn; xiaohan@hust.edu.cn; zychen@hust.edu.cn).

Wei Xu and Yirong Tang are with the State Key Laboratory of High Density Electromagnetic Power and Systems, Institute of Electrical Engineering, Chinese Academy of Sciences, Beijing 100190, China., and also with the School of Electronic, Electrical and Communication Engineering, University of Chinese Academy of Sciences, Beijing 101408, China. (e-mail: weixu@mail.iee.ac.cn; yirtang@mail.iee.ac.cn).

Ion Boldea is with Electrical Engineering Department, Politehnica University Timisoara, 300223 Timisoara, Romania. (e-mail: ion.boldea@upt.ro).

Color versions of one or more figures in this article are available at https://doi.org/10.1109/TPEL.2026.3653059.

Digital Object Identifier 10.1109/TPEL.2026.3653059

I. Introduction

URBAN rail transit driven by linear induction machines (LIMs) has been fast developed in recent years and commercialized in more than 20 linear metro lines around the world due to its merits of strong climbing ability, small turning radius, small cross-sectional area, and so on [1], [2]. Considering the installation limitation and maintenance cost, the speed sensor is unavailable to such urban rail transit. Thereof, the speed sensorless control of LIM adopted to linear metro has attracted more and more attention by both academia and industry [3].

However, the special structure of LIM, such as cut-open of primary iron core, would lead to some end effects during the operation, i.e., the air-gap flux usually goes down with the rising speed, resulting in a drastic nonlinear change of equivalent mutual inductance versus various speed, especially in the high-speed flux-weakening (FW) region [4]. Generally, the accuracy of observed speed depends on the performance of flux and speed observation modules. Since the conventional observation modules mostly rely on accurate parameters of LIM, as easily affected by the end effect, it may finally lead to the large steady-state error of speed observation. Therein, the scholars around the world are dedicated to improving the accuracy and robustness of flux and speed modules.

On one hand, to improve the precision of flux observation, many advanced flux observers have been proposed till now [5], [6], [7], [8]. Among them, the SMO has been extensively adopted in the ac motor control system owing to its simple structure and strong robustness, especially suitable for LIM with severe nonlinear parameter variations. In [5], a flux observer based on improved high order sliding mode is presented to obtain the accurate observed flux of rotatory induction machine (RIM). To deal with the uncertainties caused by parameter variation, a terminal sliding mode rotor flux observer is proposed in [6] to obtain a better observation performance in terms of rapidness and robustness. In [7], a time-varying state observer based on twisting control is proposed to implement the precise flux observation. To enhance the robustness of flux observer against the parameter variation, a super-twisting flux observer with disturbance compensation term is proposed in [8]. Nevertheless, the output injections of the flux observers aforementioned are coupled with mutual inductance, where the observation accuracy of flux would be reduced with the speed going up. Moreover,

the flux observers mentioned above mainly work below the rated speed of LIM, rather than in the high-speed FW region, where the more serious nonlinear change of mutual inductance will occur and the accuracy of flux observer will be decreased.

On the other hand, to enhance the speed observation accuracy under parameter nonlinear change, more and more advanced sensorless control methods have been proposed in recent years. In these methods, non-model-based methods attract a lot of attention due to the independence on the accurate model of LIM [9], [10], [11], [12]. The speed signal can be extracted through the injection of additional signals. However, when the LIM operates in the high-speed FW region, the additional signal injections will bring extra disturbance to the control system, causing the degradation of dynamic performance and even instability of the control system. Moreover, the additional signals will produce inevitable loss and thrust fluctuation, reducing the operation efficiency and comfort of urban rail transit. Thereof, the non-model-based methods are not suitable for the LIM senosrless control system in urban rail transit. Another popular kind of speed observation method is the model-based method, which contains two main kinds of speed observation techniques: phase locked loop (PLL)-based method and speed adaptive law method. The PLL-based method has been widely used in speed observation with various advanced PLL structure [13], [14]. To obtain the accurate estimated speed of LIM, a novel double PLL structure is proposed in [13] with the aim of acquiring the accurate synchronous angular frequency. However, due to that the speed observation depends closely on mutual inductance, as directly influenced by end effect, the speed steady-state error will become much larger in the high-speed FW region. In general, for the speed adaptive law method, various kinds of speed observers are constructed to realize the speed estimation, such as model reference adaptive system (MRAS) [15], [16], [17], adaptive full-order observer [18], [19], [20], sliding mode observer (SMO) [6], [21], [22], [23], [24], and so on. Similar to the flux observer, the accuracy of the speed adaptive law-based method depends on the parameters, which also requires the strong robustness against the severe parameter variation of the speed observer. The terminal SMO is proposed in [6] to enhance the robustness against the parameter variation. In [21], a super-twisting sliding mode speed observer is proposed to acquire the accurate estimated speed with a twisting convergence trajectory. However, the mutual inductance still exists in the speed adaptive law, which will decrease the accuracy of speed estimation, especially in the high-speed FW region. In [22], combined with MRAS, a second-order SMO-based speed observation is proposed, effectively improving the robustness of the control system. To further strengthen the robustness against the serious parameter variation, the SMO-based MRAS speed estimation with online identification strategy is proposed in [23] and [24]. The observation accuracy of speed under these methods aforementioned depends on the accuracy of mutual inductance in reference model. However, it is difficult to obtain the precise parameters of LIM in practice, which may lead to an unsatisfied observation performance of speed adaptive law method.

Thereof, in order to increase the observation performance of LIM sensorless control system in terms of rapidness, accuracy and robustness against parameter variation, an improved speed sensorless control strategy for LIM based on full order terminal sliding mode (FOTSM) with adaptive gain is proposed in this article.

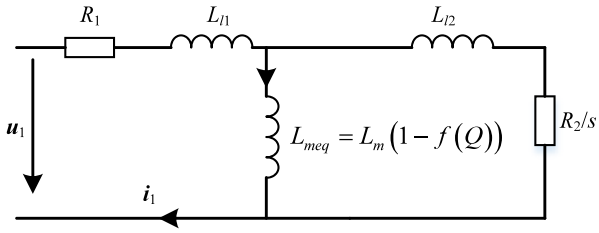

Fig. 1. T-type equivalent circuit of the LIM [25].

The rest of this article is organized as follows. The mathematical model and FW operation principle of LIM are fully introduced in Section II. The proposed speed sensorless control strategy based on FOTSM is detailed in Section III. Comprehensive simulation and experimental results are presented in Sections IV. Finally, Section V concludes this article.

II. LIM Model and FW Operation

A. LIM Model

One typical T-type equivalent circuit of LIM proposed by Duncan [25] is shown in Fig. 1. The specific characteristic of LIM, end effect, is considered by end effect factor, as given by

$$f(Q) = \frac{1 - e^{-Q}}{Q}, Q = \frac{lR_2}{v_2(L_m + L_{l2})} \tag{1}$$

where v_2 is the secondary speed, l the motor effective length, R_2 the secondary resistance, L_m the static value of mutual inductance, and L_{l2} the secondary leakage inductance. As seen from Fig. 1, the mathematical model of LIM under secondary flux orientation in the reference frame is expressed by

$$\begin{cases} \dot{\boldsymbol{i}}_1 = \frac{\xi}{T_2} K\boldsymbol{\psi}_2 - K\xi\omega_2 \boldsymbol{J}\boldsymbol{\psi}_2 - \lambda \boldsymbol{i}_1 - \omega_1 \boldsymbol{J}\boldsymbol{i}_1 + K\boldsymbol{u}_1 \\ \dot{\boldsymbol{\psi}}_2 = \frac{L_{meq}}{T_2}\boldsymbol{i}_1 - \frac{1}{T_2}\boldsymbol{\psi}_2 - (\omega_1 - \omega_2)\boldsymbol{J}\boldsymbol{\psi}_2 \end{cases}$$
$$\sigma = 1 - \frac{L_{meq}^2}{L_1 L_2}, \lambda = \frac{R_1 L_2^2 + R_2 L_{meq}^2}{\sigma L_1 L_2}$$
$$\xi = \frac{L_{meq}}{L_2}, K = \frac{1}{\sigma L_1}, \boldsymbol{J} = \begin{bmatrix} 0 & -1 \\ 1 & 0 \end{bmatrix} \tag{2}$$

where $\boldsymbol{i}_1 = [i_{1d}, i_{1q}]^T$ is the primary current vector, $\boldsymbol{u}_1 = [u_{1d}, u_{1q}]^T$ the primary voltage vector, $\psi_2 = [\psi_{2d}, \psi_{2q}]^T$ the secondary flux vector, T_2 the secondary time constant, $L_{meq} = L_m(1\text{-}f(Q))$ equivalent mutual inductance, R_1 and $L_1 = L_{meq}+L_{l1}$ are the primary resistance and inductance, $L_2 = L_{meq}+L_{l2}$ the inductance, L_{l1} the primary leakage inductance, ω_1 and ω_2 the synchronous and secondary angular frequency.

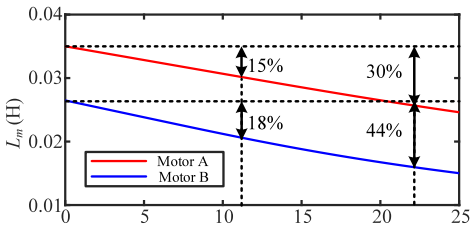

Fig. 2. Range of L_m variation with the change of speed.

B. FW Operation

The voltage of LIM in d–q axis can be expressed as

$$\begin{cases} u_{1d} = R_1 i_{1d} + \sigma L_1 \dot{i}_{1d} - \omega_1 \sigma L_1 i_{1q} + \xi \dot{\psi}_{2d} \\ u_{1q} = R_1 i_{1q} + \sigma L_1 \dot{i}_{1q} + \omega_1 \sigma L_1 i_{1d} + \omega_1 \xi \psi_{2d} \end{cases}. \tag{3}$$

When the LIM works in the high-speed steady-state condition, the voltage drop of the primary resistance, the derivatives of secondary flux and primary current are ignored. Thereof, (3) can be transformed into

$$\begin{cases} u_{1d} = -\omega_1 \sigma L_1 i_{1q} \\ u_{1q} = \omega_1 L_1 i_{1d} \end{cases}. \tag{4}$$

The thrust F_e is expressed as

$$F_e = \frac{3\pi L_{meq}^2}{2\tau L_2} i_{1d} i_{1q} \tag{5}$$

where τ is the pole distance.

For the working safety in the FW region, the constraints of the voltage, current and slip frequency must be satisfied simultaneously, as given by

$$\begin{cases} i_{1d}^2 + i_{1q}^2 \le i_{1\max}^2 \\ (\omega_1 \sigma L_1 i_{1q})^2 + (\omega_1 L_1 i_{1d})^2 \le u_{1\max}^2 \\ |u_{1d}| \le u_{1\max}/\sqrt{2} \end{cases} \tag{6}$$

where $u_{1\max}$ and $i_{1\max}$ are the maximum voltage and current.

However, the optimal voltage vector can be obtained only when flux observation is accurate. The mutual inductance in the LIM changes along with the speed, which means there will be an error of flux orientation in the FW region. Fig. 2 shows the range of mutual inductance variation with the change of speed. It can be seen that the value of mutual inductance would be decreased by 15% and 18% at 11 m/s (rated speed) and 30% and 44% at 22 m/s for two prototyped LIMs (parameters of Motor A and B will be shown in Appendix C). It can be indicated that parameter variation becomes more severe when LIM operates in high-speed FW region. This will decrease the accuracy of flux orientation. To better analyze the impact of parameter variation on LIM, the derivation process is given out.

Considering the flux orientation error δ caused by the parameter mismatch, it can be derived that

$$\begin{bmatrix} i_{1d} \\ i_{1q} \end{bmatrix} = \begin{bmatrix} \cos\delta & -\sin\delta \\ \sin\delta & \cos\delta \end{bmatrix} \begin{bmatrix} i'_{1d} \\ i'_{1q} \end{bmatrix} \tag{7}$$

where i'_{1d} and i'_{1q} are d–q axis currents under inaccurate FOC.

Fig. 3 shows the constraints of the primary currents and voltages. The blue dotted lines and black solid lines represent

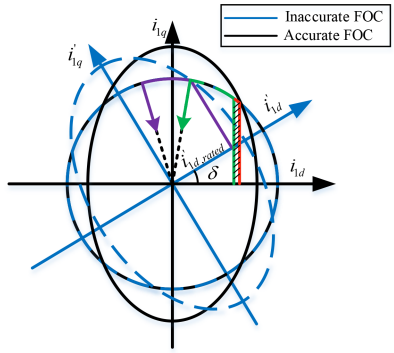

Fig. 3. Constraints of the primary currents and voltages under the accurate and inaccurate flux orientation.

the constraints under the inaccurate and accurate flux orientation, respectively. The purple and green solid lines represent the trajectory of current vectors in full speed region. It can be observed that the rated d-axis current in the accurate flux orientation is equal to

$$i_{1\mathrm{drated}} = i'_{1\mathrm{drated}} \cos\delta - i'_{1q} \sin\delta \tag{8}$$

which means that the LIM cannot work in the shaded region.

Substituting (7) into (5), it yields

$$F_e = \frac{3\pi L_{meq}^2}{2\tau L_2} i_{1d} i_{1q} \cos 2\delta + \frac{3\pi L_{meq}^2 \left(i_{1d}^2 - i_{1q}^2\right)}{4\tau L_2} \sin 2\delta. \tag{9}$$

It can be seen that the thrust expression considering the flux orientation error in (9) is composed of two parts, including common term and coupled term. When the error is rather small, the approximation condition can be got by

$$\cos 2\delta \approx 1,\ \sin 2\delta \approx 0. \tag{10}$$

Therein, the second part in (9) can be ignored, which would be the same as (5). With the enlarging flux orientation error, the approximation condition mentioned above is not reasonable. It should be noticed that the double value of the flux orientation error exists in the trigonometric function, which means that the influence of the error is amplified. The thrust would be severely decreased by the error under the inaccurate flux orientation.

III. Robust Speed Sensorless Control

To minimize the use of the parameters related to end effect, the EMF-primary current model in α–β axis and the active flux-primary current model in d–q axis are chosen for flux and speed estimation, respectively. And the improved FOTSM observer is constructed based on the two models to enhance robustness against the parameter variation.

A. FOTSM Observer for Active Flux

Traditional flux observers are primarily designed based on current models to estimate secondary flux. However, the accuracy of these observers is highly sensitive to secondary-side parameters, which brings significant challenges for the application in LIM characterized by nonlinear parameter variations. In

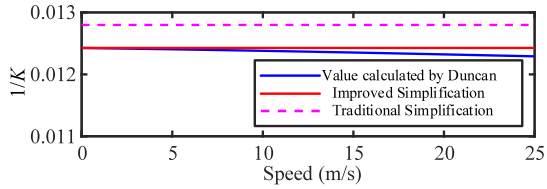

Fig. 4. Analysis of σL1 simplification with the change of speed.

contrast, flux observers based on voltage models are independent of secondary-side parameters, which is more suitable for LIM sensorless control system. According to the T-type equivalent circuit of LIM in Fig. 1, the secondary EMF-primary current model in α–β axis is described as

$$\dot{\boldsymbol{i}}_{1\alpha\beta} = K\left(\boldsymbol{u}_1 - R_1\boldsymbol{i}_{1\alpha\beta} + \xi\boldsymbol{e}_2\right) \tag{11}$$

where $\boldsymbol{e}_2$ represents the secondary EMF. It can be seen that the coefficient K and ξ, affected by end effect, are used in the secondary EMF-primary current model. Fig. 4 shows that this coefficient $1/K$ hardly changes with the speed increasing. Generally, this coefficient can be simplified as L_{l1}+L_{l2} in RIM considering that the ratio between mutual inductance and leakage inductance is large. However, it is not suitable for LIM due to the ratio between mutual inductance and leakage inductance is relatively small. Thereinto, an improved simplification method for LIM is employed [26] to avoid model parameters with end effect, as given by

$$\frac{1}{K} = L_{l1} + \frac{L_{l2}L_m}{L_{l2} + L_m}. \tag{12}$$

To deal with another coefficient ξ affected by end effect in the secondary EMF-primary current model, the observed quantity is chosen as the back EMF, rather than secondary back EMF, which is defined as

$$\boldsymbol{e}_m = \frac{d\boldsymbol{\psi}_m}{dt} = \xi\frac{d\boldsymbol{\psi}_2}{dt} \tag{13}$$

where ψ_m is named as active flux [27]. It can be seen that the active flux and the secondary flux share the same phase, differing only in amplitude. Therefore, the active flux orientation control can achieve a same control performance compared to that of secondary flux orientation control.

To obtain the back EMF, an FOTSM observer is designed as

$$\dot{\hat{\boldsymbol{i}}}_{1\alpha\beta} = K\left(\boldsymbol{u}_1 - R_1\hat{\boldsymbol{i}}_{1\alpha\beta} + \boldsymbol{w}\right) \tag{14}$$

where $\|\boldsymbol{e}_m\| \le G_e = \omega_1\|\psi_m\|$ and $\|\dot{\boldsymbol{e}}_m\| \le G_{de} = {\omega_1}^2\|\psi_m\|$.

Then, subtracting (11) from (14), the error dynamics of primary currents can be obtained by

$$\Delta\dot{\boldsymbol{i}}_{1\alpha\beta} = K\left(-R_1\Delta\boldsymbol{i}_{1\alpha\beta} + \boldsymbol{w} - \boldsymbol{e}_m\right). \tag{15}$$

To achieve a satisfying dynamic performance of the observer in terms of the accuracy, rapidness and robustness, an FOTSM manifold is constructed as

$$\mathbf{s}_\psi = \Delta\dot{\boldsymbol{i}}_{1\alpha\beta} + \boldsymbol{C}_1\Delta\boldsymbol{i}_{1\alpha\beta}^{p/q} + \boldsymbol{C}_2\mathrm{sgn}\left(\Delta\boldsymbol{i}_{1\alpha\beta}\right) \tag{16}$$

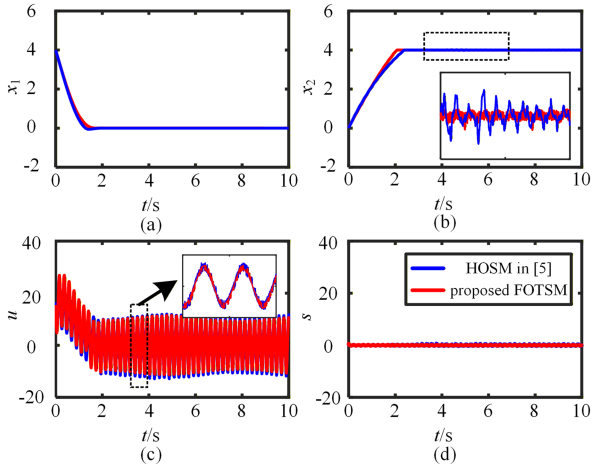

Fig. 5. Comparison between FOTSM and HOSM. (a) State variable x_1. (b) State variable x_2. (c) Control input u. (d) Sliding manifold s.

where $\boldsymbol{s}_\psi = [s_{\psi\alpha}, s_{\psi\beta}]^T$, $\boldsymbol{C}_1 = \mathrm{diag}(C_{1\alpha}, C_{1\beta})$, and $\boldsymbol{C}_2 = \mathrm{diag}(C_{2\alpha}, C_{2\beta})$ are positive matrixes, p and q positive odds that meet $0<p/q<1$. In order to better elaborate the superiority of the proposed FOTSM, full comparison between FOTSM and high-order sliding mode (HOSM) [5] is made. As seen from Fig. 5, state variables of FOTSM can converge to zero faster than those of HOSM owing to the introduce of terminal attractor, and the convergency accuracy of variables under FOTSM is more precise. Moreover, output injections of FOTSM are smoother, which means the chattering can be effectively attenuated. Thereof, FOTSM has a slight advantage in performance compared to HOSM.

The output injection of the observer can be designed as

$$\begin{cases} \boldsymbol{w} = \boldsymbol{w}_{eq} + \boldsymbol{w}_n \\ \boldsymbol{w}_{eq} = R_1\Delta\boldsymbol{i}_{1\alpha\beta} - \left(\boldsymbol{C}_1\Delta\boldsymbol{i}_{1\alpha\beta}^{p/q} + \boldsymbol{C}_2\mathrm{sgn}\left(\Delta\boldsymbol{i}_{1\alpha\beta}\right)\right)/K \\ \boldsymbol{w}_n = \int\left(-k_1\boldsymbol{s}_\psi - k_2\mathrm{sgn}\left(\boldsymbol{s}_\psi\right)\right)dt/K \end{cases} \tag{17}$$

where k_1 and k_2 are positive constants. To further attenuate the chattering, an adaptive control gain k_2 is designed as

$$k_2 = |\hat{\omega}_1|^2\eta + \varepsilon \tag{18}$$

where $\eta > {L^2}_m i_{1\,d,\mathrm{rated}}/L_2$, $\varepsilon > 0$. The stability analysis of flux observer is listed in Appendix A. When the LIM operates in the low-speed region, the parameter variation is not relatively severe, and the adaptive control gain would be small to suppress the chattering. In high-speed FW region, the adaptive control gain can be large enough to satisfy the Lyapunov stability condition.

From the derivation aforementioned, the state variables of the observer can converge to zero in the finite time, which means the equivalent control law $\boldsymbol{w}_{\mathrm{eq}}$ can be forced to converge to zero. Meanwhile, owing to the integral-type control law $\boldsymbol{w}_n$, the chattering in the conventional SMO can be effectively attenuated and the output signals of the FOTSM observer are smooth and continuous.

The estimated active flux can be obtained by integrating the estimated back EMF. To avoid the influence of the dc offset to the

observation, a second order generalized integrator is employed to estimate both active flux and synchronizing frequency.

B. Robust Speed Estimation Scheme

According to the estimated speed mentioned in the existing methods [6], [13], the speed expression can roughly be divided into the following two types:

$$\hat{\omega}_2 = \hat{\omega}_1 - \omega_{sl}, \omega_{sl} = L_{meq} i_{1q} / T_2 \psi_{2d}$$
$$\hat{\omega}_2 = \left(\hat{\psi}_{2\beta} w_\alpha - \hat{\psi}_{2\alpha} w_\beta\right) / \left(K\xi \left\|\hat{\boldsymbol{\psi}}_{2\alpha\beta}\right\|^2\right) \tag{19}$$

where ω_{sl} is the slip angular frequency.

It can be inferred from (19) that the mutual inductance is contained in both expressions, which indicates that the accuracy of speed estimation would be decreased with speed going up. When the LIM system operates in a high-speed FW region, the steady-state error will occur between the estimated and actual speeds. In general, some speed observers in the existing literatures are constructed in α–β axis, where the accuracy would be decreased due to the couple between secondary time constant and flux. Thereof, the speed observer in this article will be constructed in *d*-*q* axis to implement minimum use of parameters affected by end effect.

Given parameter variations caused by end effect, it will get

$$L_{meq} = L_{meq} + \Delta L_{meq}, T_2 = T_2 + \Delta T_2. \tag{20}$$

Accordingly, relative parameter variations are shown as

$$\xi = \xi_0 + \Delta\xi, \lambda = \lambda_0 + \Delta\lambda, K = K_0 + \Delta K. \tag{21}$$

The parameter variations aforementioned are assumed as upper-bounded, as given by

$$|\Delta\xi| \le M_\xi, |\Delta\lambda| \le M_\lambda, |\Delta K| \le M_K. \tag{22}$$

Thereof, the primary current dynamics (2a) is expressed as

$$\dot{\boldsymbol{i}}_{1dq} = K\mathbf{M} - \lambda \boldsymbol{i}_{1dq} - \omega_1 \boldsymbol{J} \boldsymbol{i}_{1dq} + K \boldsymbol{u}_{1dq} \tag{23}$$

where $\boldsymbol{M} = \boldsymbol{\psi}_m / T_2 - \omega_2 \boldsymbol{J} \boldsymbol{\psi}_m$. It can be seen that the speed signals exist in $\boldsymbol{M}$. To acquire the speed, an improved FOTSM observer is designed in *d*-*q* axis by estimating $\boldsymbol{M}$, as shown by

$$\dot{\hat{\boldsymbol{i}}}_{1dq} = K_0 \boldsymbol{\gamma} - \lambda_0 \hat{\boldsymbol{i}}_{1dq} - \omega_1 \boldsymbol{J} \hat{\boldsymbol{i}}_{1dq} + K_0 \boldsymbol{u}_{1dq}. \tag{24}$$

Subtracting (23) from (24), it yields

$$\Delta\dot{\boldsymbol{i}}_{1dq} = K_0 \boldsymbol{\gamma} - \lambda_0 \Delta \boldsymbol{i}_{1dq} - \omega_1 \boldsymbol{J} \Delta \boldsymbol{i}_{1dq} - \boldsymbol{d}_i \tag{25}$$

where $\boldsymbol{d}_i = \boldsymbol{d}_{i1} + \boldsymbol{d}_{i2} + \boldsymbol{d}_{i3} = -\Delta\lambda \boldsymbol{i}_1 - K\mathbf{M} + \Delta K \boldsymbol{u}_1$.

For better understanding on $\boldsymbol{d}_i$, the boundaries of uncertainties are expressed by

$$\begin{aligned}
&\|K\boldsymbol{M}\| \le G_M,\ \|\lambda_0 \boldsymbol{i}_1\| \le G_i,\ \|K_0 \boldsymbol{u}_1\| \le G_u \\
&\|\boldsymbol{e}_m / T_2\| \le G_E,\ \|\omega_2 \boldsymbol{J} \boldsymbol{e}_m\| \le G_{\omega E},\ \|\boldsymbol{i}_1\| \le I_{1\max}, \\
&\quad \|\boldsymbol{u}_1\| \le u_{1\max} \\
&\|\boldsymbol{W}\boldsymbol{J}\mathbf{M}\| \le G_{WM}, \|\lambda_0 \boldsymbol{J}\boldsymbol{W}\boldsymbol{i}_1\| \le G_{Wi}, \\
&\quad \|K_0 \boldsymbol{J}\boldsymbol{W}\boldsymbol{u}_1\| \le G_{Wu}.
\end{aligned} \tag{26}$$

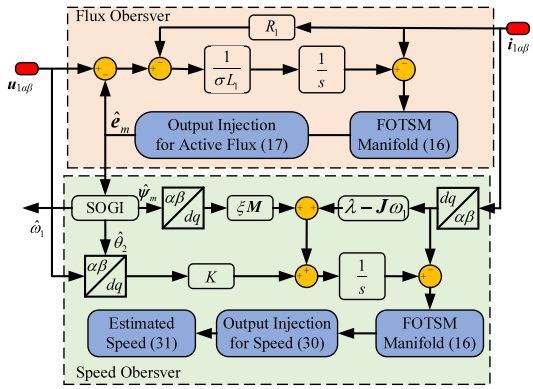

Fig. 6. Block diagram of the proposed FOTSM observer.

The upper-boundary and its derivative of $\boldsymbol{d}_i$ are expressed as

$$\begin{aligned}
&\|\boldsymbol{d}_i\| \le |\Delta\lambda| \|\boldsymbol{i}_1\| + \|K\boldsymbol{M}\| + |\Delta K| \|\boldsymbol{u}_1\| \\
&= M_\lambda I_{1\max} + G_M + M_K u_{1\max} = G_0
\end{aligned} \tag{27}$$

$$\begin{aligned}
\left\|\dot{\boldsymbol{d}}_{i1}\right\| &\le M_\lambda \left(G_M + G_i + G_u\right) = G_{d1} \\
\left\|\dot{\boldsymbol{d}}_{i2}\right\| &\le M_K \left(G_E + G_{\omega E}\right) = G_{d2} \\
\left\|\dot{\boldsymbol{d}}_{i3}\right\| &\le M_K \left(G_{WM} + G_{Wi} + G_{Wu}\right) = G_{d3}.
\end{aligned} \tag{28}$$

Thereof, the derivatives are upper-bounded, as given by

$$\left\|\dot{\boldsymbol{d}}_i\right\| \le G_{d0}, G_{d0} = G_{d1} + G_{d2} + G_{d3}. \tag{29}$$

The full-order sliding manifold $\mathbf{s}_v$ is also selected from (16). Then the output injections of speed observer are designed by

$$\begin{cases}
\boldsymbol{\gamma} = \boldsymbol{\gamma}_{\text{eq}} + \boldsymbol{\gamma}_n \\
\boldsymbol{\gamma}_{\text{eq}} = \lambda_0 \Delta \boldsymbol{i}_{1dq} + \omega_1 \boldsymbol{J} \bar{\boldsymbol{i}}_{1dq} - \boldsymbol{C}_1 \Delta \boldsymbol{i}_{1dq}^{p/q} - \boldsymbol{C}_2 \text{sgn}\left(\Delta \boldsymbol{i}_{1dq}\right) \\
\boldsymbol{\gamma}_n = \int \left(-k_3 \boldsymbol{s}_v - k_4 \text{sgn}\left(\boldsymbol{s}_v\right)\right) dt
\end{cases} \tag{30}$$

where $\gamma = [\gamma_d, \gamma_q]^T$, k_3 and k_4 are control gains, satisfying $k_3 > 0$ and $k_4 > 0$.

It is noted that, Lyapunov stability proof of the speed observer is not made here for its similarity to that of the flux observer, as discussed in Appendix. In the accurate flux orientation, the *q*-axis secondary flux is equal to zero, and the estimated speed can be expressed as

$$\hat{v}_2 = -\tau\gamma_q / \left(\pi \hat{\psi}_{md}\right). \tag{31}$$

Fig. 6 shows the block diagram of the proposed speed sensorless control based on FOTSM. It is concluded that the estimated speed can be obtained directly from the output injection of FOTSM observer when the synchronous angular frequency and amplitude of active flux are acquired precisely from the flux observer. Due to the minimum use of parameters affected by end effect and integral-type sliding mode output injections, the estimated speed possesses a strong robustness against parameter variation, which can track the actual speed more accurately. Fig. 7 shows the overall block diagram of LIM speed sensorless control.

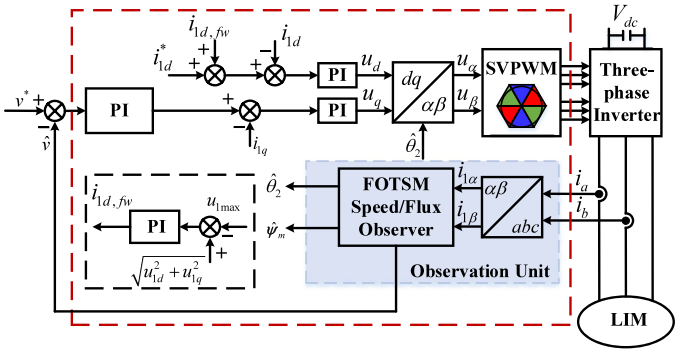

Fig. 7. Diagram of LIM speed sensorless control.

IV. Simulation and Experimental Results

In order to demonstrate the effectiveness of the proposed speed sensorless control based on the proposed FOTSM, comprehensive simulation and experimental studies have been carried out in this section. The conventional SMO [6], MRAS-HOSM-based method [5] and PLL-based method [13] are adopted to compare with the proposed method.

A. Simulation Results

The related simulations are conducted on 12000-Type LIM (motor B), as popularly adopted to actual linear metro. Main parameters are summarized in Table III of Appendix C. The reference speed is initially set as 11 m/s and changed to 22 m/s at 6 s. The speed, active flux, and position are shown in Fig. 8. As can be seen from this figure, the estimated speeds under all sensorless methods can quickly track the actual value. However, due to the inherent chattering in the output injection, there is a relatively large speed fluctuation in the speed estimation of the conventional SMO and the speed estimation accuracy is not satisfactory. Meanwhile, the accuracy of estimated speed under MRAS-HOSM-based method is decreased with speed increasing due to the mutual inductance in the reference model. By comparing the PLL-based method with the proposed method, both methods can obtain the accurate speed estimation under the relatively low speed. However, the disparity between calculated and actual values of ω_{sl} is substantial with the increasing speed, leading to a steady-state error. Even though some other nonlinear changed parameters related to end effect are not considered in the LIM model, such as secondary resistance, the proposed FOTSM observer still benefits a superior observation performance in terms of rapidness, accuracy and robustness against parameter variation owing to integral type control law and adaptive gain.

Fig. 8(b) and (c) also shows the observed flux and phase waveforms of the proposed method. The estimated active flux can track the actual flux precisely and rapidly, which means the phase of the estimated active flux is also accurate. Thereinto, it can be concluded that the flux observation accuracy is high under the proposed FOTSM observer.

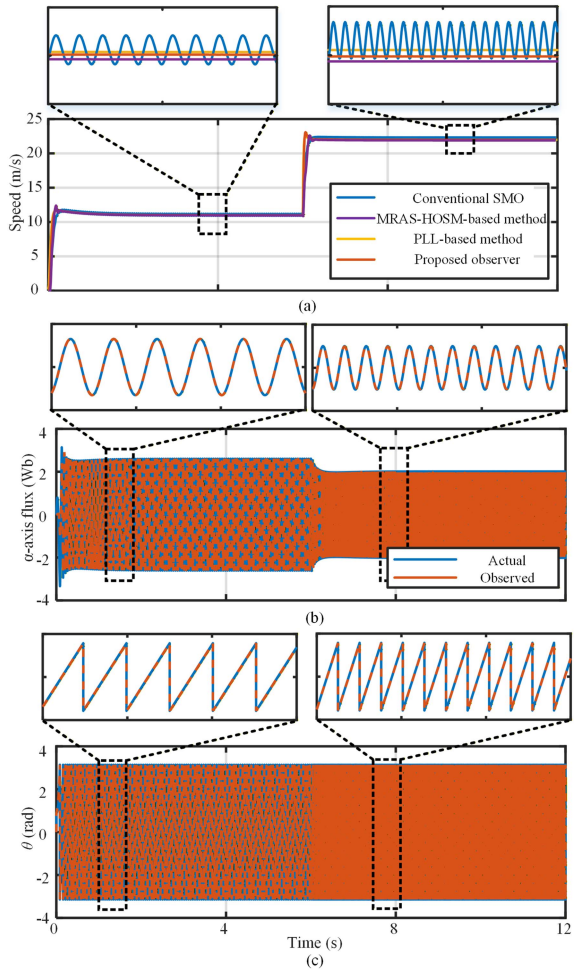

Fig. 8. Performance analysis under variable speeds. (a) Speed. (b) α-axis active flux. (c) Active flux phase.

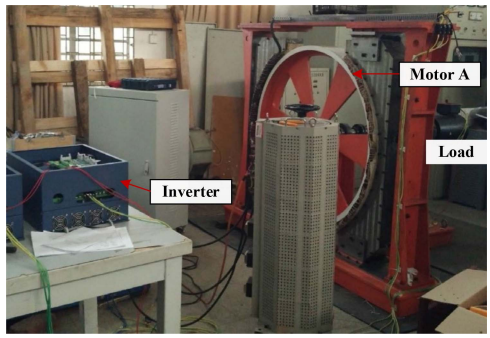

Fig. 9. Arc induction machine platform.

B. Experimental Results

To verify the proposed method, extensive experiments are conducted on a 3 kW arc induction machine (motor A) platform, as shown in Fig. 9. The testing system consists of motor A and a permanent magnet synchronous generator (PMSG). Motor A is coaxially coupled to the PMSG via a gearbox. The PMSG is connected to a resistance box through a voltage regulator. By adjusting the transformation ratio of the voltage regulator, the energy dissipated by the resistance box can be controlled,

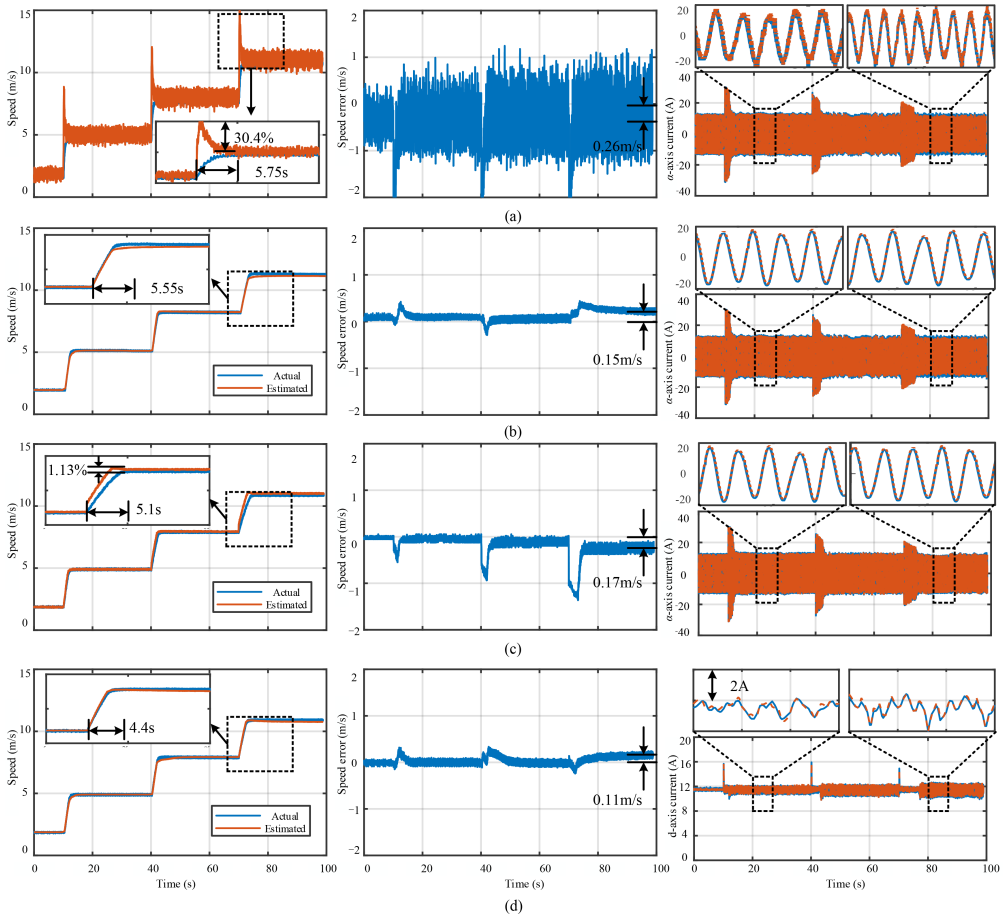

Fig. 10. Dynamic performance of different sensorless control methods in low-medium speed region. (a) Conventional SMO. (b) MRAS-HOSM-based method. (c) PLL-based method. (d) Proposed method.

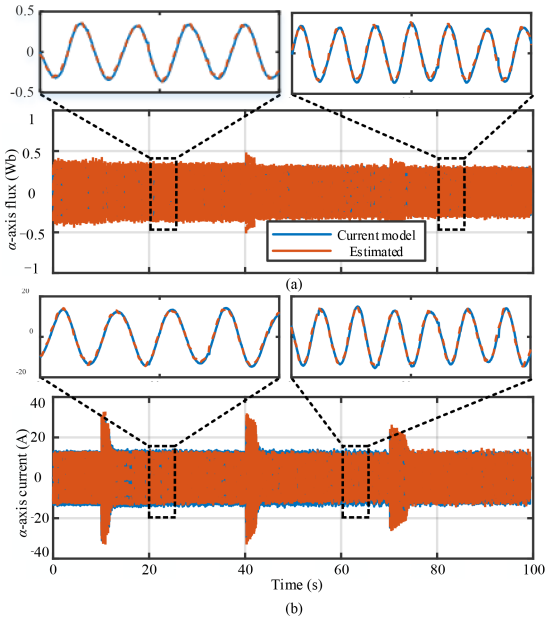

Fig. 11. Active flux estimation in low-medium speed region. (a) α-axis active flux. (b) α-axis current.

thereby achieving flexible regulation of the load force. Main parameters of motor A are given in Table II of Appendix C.

1) Case I: Dynamic Performance in Low-Medium Speed Region: Fig. 10 shows the dynamic performance of different sensorless control methods at various speeds below the rated speed. The reference speed is set as 2 m/s, and changed to 5 m/s at 10 s, and then to 8 m/s at 40 s, and finally to 11 m/s at 70 s. The load force is set as 50 N. As can be seen from Fig. 10, the estimated speed of conventional SMO can only track the actual speed with a large overshoot and oscillation. The reason for the severe speed fluctuation and overshoot is that the sign function exists in the output injection of the SMO, thereinto leading to the high frequency chattering in the estimated speed. Fig. 10 also shows that the estimated speed of the MRAS-HOSM-based method can track the actual speed quickly. However, with the speed increasing, the steady-state error between the actual and estimated speeds becomes larger due to the mutual inductance in the speed adaptive law. Similarly, the PLL-based method can obtain the accurate speed estimation under the relatively low speed. Nevertheless, the disparity between the calculated and actual values of ω_{sl} is substantial with the speed increasing, which leads to decreasing the dynamic performance in terms of overshoot and accuracy.

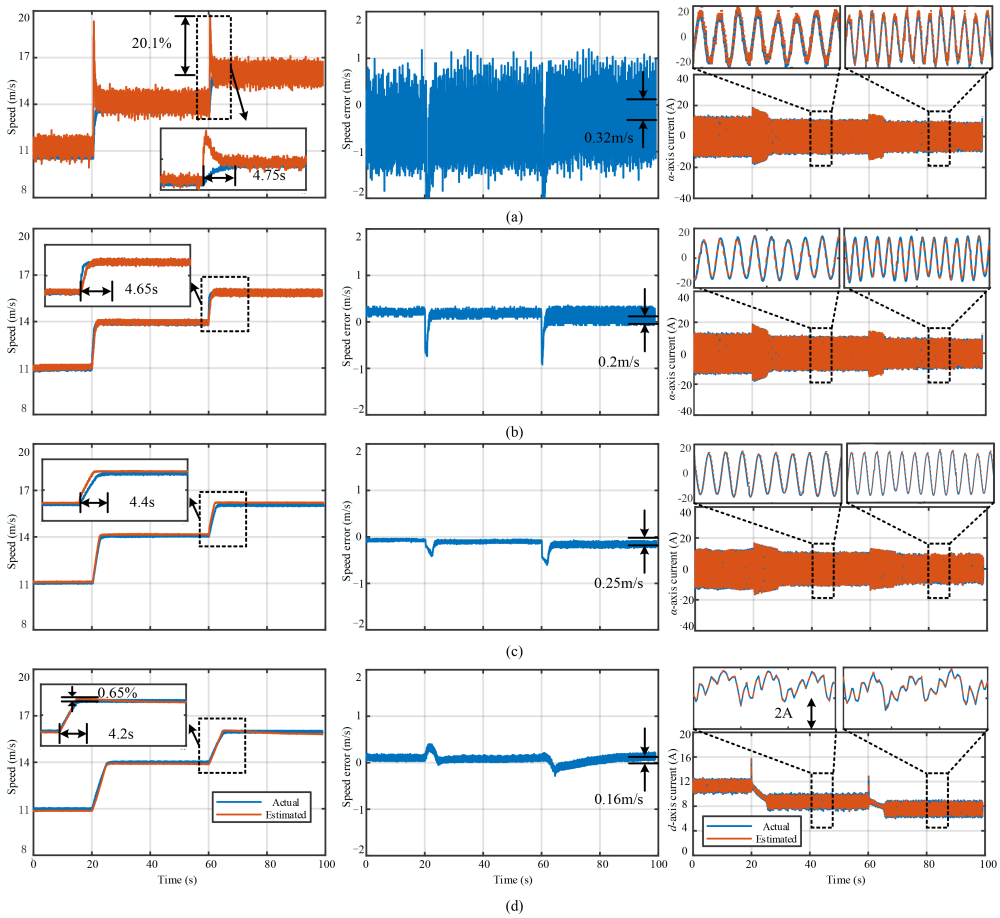

Fig. 12. Dynamic performance of different sensorless control methods in high-speed FW region. (a) Conventional SMO. (b) MRAS-HOSM-based method. (c) PLL-based method. (d) Proposed method.

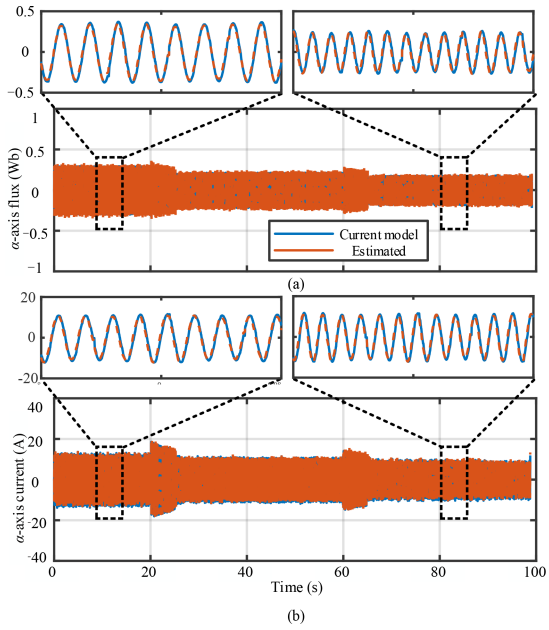

Fig. 13. Active flux estimation in high-speed FW region. (a) α-axis active flux. (b) α-axis current.

In contrast, from Fig. 10, it is obvious that the estimated speed of the proposed FOTSM observer can track the actual speed quickly and precisely with small steady-state error and fast dynamic response, owing to the advantage of rapidness and stability brought by the finite-time convergence of the terminal sliding mode and minimum use of the parameters affected by end effect in the observer design. Even though secondary resistance is not taken into consideration in the LIM model, the proposed FOTSM observer still possesses a superior observation performance in terms of rapidness, accuracy and robustness against parameter variation owing to integral type control law and adaptive gain.

From Fig. 10, the maximum speed estimation error of all methods at 11 m/s is 0.26 m/s, 0.15 m/s, 0.17 m/s and 0.11 m/s, respectively. It can be concluded that the proposed method can obtain the accurate speed in low-medium speed region. Fig. 11 shows the active flux estimation of the proposed FOTSM flux observer. Compared with the observed active flux of current model, the proposed FOTSM flux observer can accurately observe the effective flux owing to integral type control law.

2) Case II: Dynamic Performance in High-Speed FW Region: To further validate the superiority of the proposed speed sensorless control in the high-speed FW region, the speed increases further from 11 to 14 m/s and finally to 16 m/s. As can be

TABLE I
PERFORMANCE INDICES OF DIFFERENT SENSORLESS METHODS

Speed Region	Method	Over-shoot	Accuracy	Settling Time
Low-medium	Conventional SMO	30.4%	0.26 m/s	5.75 s
	MRAS-HOSM -based method	No	0.15 m/s	5.55 s
	PLL-based method	1.13%	0.17 m/s	5.1 s
	Proposed method	No	0.11 m/s	4.4 s
High	Conventional SMO	20.1%	0.32 m/s	4.75 s
	MRAS-HOSM -based method	No	0.2 m/s	4.65 s
	PLL-based method	No	0.25 m/s	4.4 s
	Proposed method	0.65%	0.16 m/s	4.2 s

seen from Fig. 12 , with the speed continuing to go up, a relatively large steady state error occurs in the speed estimation of the other three methods due to the severe parameter perturbations of LIM in the high-speed FW region. Fortunately, the steady-state performance of speed observation under the proposed method is still superior than those under the other methods owing to the strong robustness, and adaptive gain of the proposed FOTSM observer. From Fig. 12, the maximum speed estimation error at 16 m/s of the all methods in the high-speed FW region is 0.32, 0.2, 0.25 and 0.16 m/s, respectively. It can be concluded that the proposed method can also obtain the accurate speed in the high-speed FW region. Table I gives the performance indices of the different sensorless methods in both low-medium and high-speed regions. It can be concluded that the proposed method possesses a slight advantage in terms of accuracy, overshoot and rapidness by comparing to the other three methods. Fig. 13 gives the observation results of active flux. It can be seen that that the active flux can be accurately obtained compared with that of current model in terms of the phase and amplitude. The accurate flux observation is a good basis for accurate speed observation. Owing to the better performance of FOTSM in terms of accuracy, rapidness, and robustness, both flux and speed can be estimated accurately.

3) Case III: Dynamic Performance Under Speed Reversal: Fig. 14 shows the dynamic performance of the proposed method under speed reversal. The reference speed reverses from 8 m/s to −8 m/s at 40 s and then to 8 m/s at 70 s. It can be seen that the estimated speed of the proposed method can track the reference speed without overshoot and small speed fluctuation. The reason for the properties aforementioned is that the d- and q-axis currents can track their actual values rapidly and accurately. Due to the minimum use of parameters affected by end effect, the accuracy of the proposed observer is guaranteed. With the integral type control law and adaptive control gain, the chattering is effectively attenuated in the proposed FOTSM observer.

4) Case IV: Dynamic Performance Under Parameter Variation: Fig. 15 shows the dynamic performance under the parameter variation of both secondary resistance R_2 and mutual inductance L_m in 2 and 11 m/s, respectively. The R_2 changes to 130% R_2 and the L_m changes to 70% L_m at 15 s. The steady state speed errors at 2 and 11 m/s are only 0.1 and 0.13 m/s, where the speed estimation of the proposed method still possesses the high accuracy. It is due to the reason that there are still parameters

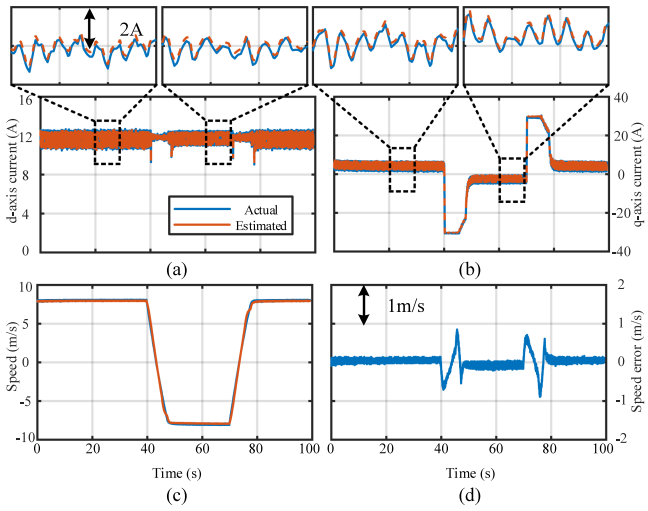

Fig. 14. Dynamic performance under speed reversal. (a) d-axis current. (b) q-axis current. (c) Speed. (d) Speed error.

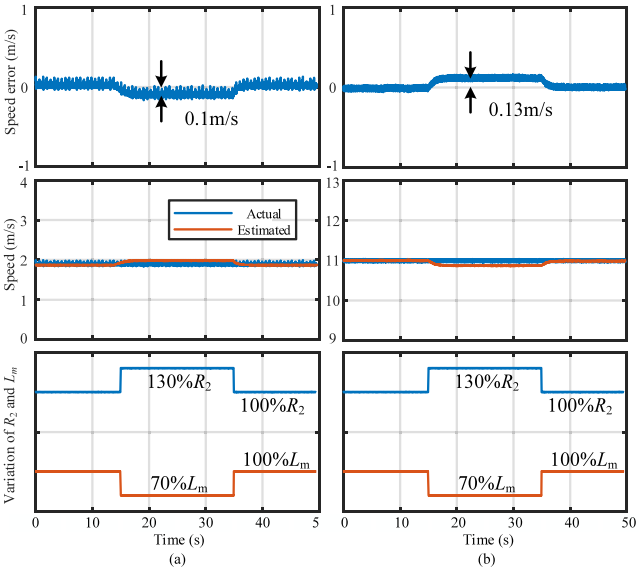

Fig. 15. Dynamic performance under parameter variation. (a) 2 m/s. (b) 11 m/s.

affected by end effect in the FOTSM observer. Owing to the strong robustness against the parameter variation, only small steady state error of speed estimation under the proposed method occurs when the parameters are perturbated. Thereinto, these experimental results demonstrate the superior performance of the proposed method under severe parameter variation.

V. CONCLUSION

In this article, an improved speed sensorless control based on FOTSM with adaptive gain is proposed to obtain the accurate speed against the severe parameter variations caused by end effect. By selecting proper state variables and coordinate system, parameter dependence affected by end effect can be apparently

reduced. Then, improved FOTSM observers with adaptive control gains are designed to enhance the accuracy and robustness. Main contributions in this article can be summarized as follows.

1) An improved FOTSM is designed to guarantee the finite time convergence of the state variables and strong robustness against the parameter variation. The integral type output injections effectively attenuate the chattering, which is beneficial to the proposed observer accuracy.
2) To minimize the use of the parameter related to the end effect, the active flux observer based on improved FOTSM is constructed in the EMF-primary current model. Then, an adaptive gain is designed by the LIM operation speed to guarantee the stability in the wide speed range.
3) To obtain the speed accurately, an improved speed observer based on improved FOTSM is proposed by designing the observer in the rotatory coordinate where the secondary time constant and flux are decoupled. The robustness against parameter variation of the estimated speed is enhanced.

APPENDIX

A. Proof of Stability of FOTSM Observer for Active Flux

In order to prove the stability of the proposed observer, the Lyapunov function is selected as

$$V_\psi = \frac{1}{2}\boldsymbol{s}_\psi^T \boldsymbol{s}_\psi. \tag{A1}$$

Combining with the primary current error dynamics (15) and the output injection of the observer (17), the FOTSM manifold can be transformed into

$$\begin{aligned}\mathbf{s}_\psi &= K\left(\boldsymbol{w} - \boldsymbol{e}_m - R_1\Delta\boldsymbol{i}_{1\alpha\beta}\right) + \boldsymbol{C}_1\Delta\boldsymbol{i}_{1\alpha\beta}^{p/q} \\ &\quad + \boldsymbol{C}_2\mathrm{sgn}\left(\Delta\boldsymbol{i}_{1\alpha\beta}\right) \\ &= \boldsymbol{w}_n - K\boldsymbol{e}_m.\end{aligned} \tag{A2}$$

Taking the derivative of V_ψ with respect to time t, it yields

$$\dot{V}_\psi = \boldsymbol{s}_\psi^T\dot{\boldsymbol{s}}_\psi = \boldsymbol{s}_\psi^T\left(\dot{\boldsymbol{w}}_n - K\dot{\boldsymbol{e}}_m\right). \tag{A3}$$

Then, combining with (17c), it gives

$$\begin{aligned}\dot{V}_\psi &= \boldsymbol{s}_\psi^T\left(-k_1\boldsymbol{s}_\psi - k_2\mathrm{sgn}\left(\boldsymbol{s}_\psi\right) + K\dot{\boldsymbol{e}}_m\right) \\ &\le -\left\|\boldsymbol{s}_\psi\right\|\left(k_1\left\|\boldsymbol{s}_\psi\right\| + k_2 - \omega_1^2\left\|\boldsymbol{\psi}_m\right\|\right).\end{aligned} \tag{A4}$$

Considering that the value of $\|\psi_m\|$ equals to $L^2{}_{\mathrm{meq}}i_{1\,d}/L_2$ in the steady state process and combing the adaptive gain (18) into (A4), it yields

$$\begin{aligned}\dot{V}_\psi &\le -\left\|\boldsymbol{s}_\psi\right\|\left(k_1\left\|\boldsymbol{s}_\psi\right\| + \hat{\omega}_1^2\eta + \varepsilon - \omega_1^2 L_{\mathrm{meq}}^2 i_{1d}/L_2\right) \\ &\le -\left\|\boldsymbol{s}_\psi\right\|\left(k_1\left\|\boldsymbol{s}_\psi\right\| + \varepsilon\right).\end{aligned} \tag{A5}$$

Thereof, the error dynamics (15) can reach the FOTSM manifold from any initial conditions in the finite time $t_{\psi r}$, as illustrated by

$$t_{\psi r} \le \max_{j=\alpha,\beta}\ln\left(2k_1V^{1/2}\left(s_{\psi j}\left(0\right)\right)/\sqrt{2}k_2 + 1\right)/k_1. \tag{A6}$$

After reaching the FOTSM manifold, the state variables of the observer can arrive at the equilibrium point in the finite time along the sliding manifold $t_{\psi s}$ as calculated by

$$t_{\psi s} \le \max_{j=\alpha,\beta}\frac{q}{(q-p)\,c_{1j}}\ln\left(c_{2j} + c_{1j}{i_{1j}}^{(q-p)/p}\right). \tag{A7}$$

Thereby, the proof has been completed.

B. Proof of Stability of LIM Closed-Loop Control System

In order to prove the closed-loop system stability of the proposed method, the overall closed-loop system can be decomposed into two distinct time-scale subsystems by adopting the singular perturbation technique [29]. The fast subsystem for the closed-loop system represents the current loop while the slow subsystem represents the speed loop and the observer. Thereinto, the completed closed-loop system in slow time scale (t) can be expressed as

$$\begin{aligned}\varepsilon\dot{\boldsymbol{x}}_f &= f_f\left(\boldsymbol{x}_f, \boldsymbol{x}_s, t\right)\ \text{Fastsubsystem} \\ \dot{\boldsymbol{x}}_s &= f_s\left(\boldsymbol{x}_f, \boldsymbol{x}_s, t\right)\ \text{Slowsubsystem}\end{aligned} \tag{A8}$$

where $\boldsymbol{x}_f = [e_{id}, e_{iq}, z_{id}, z_{iq}]^T$, $\boldsymbol{x}_s = [e_v, z_v, s_{vd}, s_{vq}, s_{\psi\alpha}, s_{\psi\beta}]^T$, ε satisfies $0<\varepsilon<<1$. Defining the following variables:

$$\begin{aligned}&e_{id} = i_d^* - i_d, e_{iq} = i_q^* - i_q, e_v = v^* - v \\ &\dot{z}_{id} = e_{id}, \dot{z}_{iq} = e_{iq}, \tilde{v} = v - \hat{v}, \dot{z}_v = e_v.\end{aligned} \tag{A9}$$

According to (2) and (A8), the dynamics of the fast subsystem can be obtained by treating the slow variables as constants in the fast time scale (εt)

$$\dot{\boldsymbol{x}}_f = \boldsymbol{A}_f\boldsymbol{x}_f + \boldsymbol{d}_f\left(\boldsymbol{x}_s\left(\varepsilon t\right), \varepsilon t\right) \tag{A10}$$

where

$$\boldsymbol{A}_f = \begin{bmatrix} -\lambda - Kk_{\mathrm{pid}} & 0 & -Kk_{\mathrm{iid}} & 0 \\ 0 & -\lambda - Kk_{\mathrm{piq}} & 0 & -Kk_{\mathrm{iiq}} \\ 1 & 0 & 0 & 0 \\ 0 & 1 & 0 & 0 \end{bmatrix}$$

$$\boldsymbol{d}_f = \begin{bmatrix} \dot{i}_d^* + \lambda i_d^* + K\xi\psi_{2d}/T_2 + \omega_1 i_{1q} \\ \dot{i}_q^* + \lambda i_q^* + K\xi\omega_2\psi_{2d} + \omega_1 i_{1d} \\ 0 \\ 0 \end{bmatrix}$$

$k_{\mathrm{pid},q}$ and $k_{\mathrm{iid},q}$ are the coefficients of PI current controllers.

By selecting appropriate PI controller gains for current loop, the fast subsystem is asymptotically stable.

The error dynamics for speed loop can be expressed by

$$\dot{e}_v = \dot{v}_{\mathrm{ref}} - \dot{v} = -\left(\frac{3\pi}{2\tau}\psi_{md}i_{1q} - F_L\right) \tag{A11}$$

where k_{pv} and k_{iv} are the coefficients of PI speed controller.

With the stability proof of fast subsystem, it can be assumed that the current loop achieves the ideal tracking ($i_{1\,q} \approx i_{1\,q}{}^*$). The error dynamics of speed loop can be transformed into

$$\begin{aligned}\dot{e}_v &\approx -\left(\frac{3\pi}{2M\tau}\left\|\psi_m\right\|i_{1q}^* - F_L\right) \\ &= -\left[\frac{1}{M}K_T\left\|\psi_m\right\|\left(k_{pv}\left(e_v + \tilde{\omega}\right) + k_{iv}z_v\right) - \frac{1}{M}F_L\right]\end{aligned} \tag{A12}$$

where $K_T = \frac{3\pi}{2\tau}\|\boldsymbol{\psi}_m\|$.

The coefficients of speed PI controllers are designed to satisfy the following conditions:

$$\begin{cases} k_{pv} > \kappa_1 \\ \frac{\varepsilon_2}{2} K_T k_{iv} - \frac{\varepsilon_4}{2} > \kappa_2 \end{cases} \tag{A13}$$

where κ_1 and κ_2 are positive.

The Lyapunov function [30] for the slow subsystem is selected as

$$V_{\text{slow}} = \underbrace{\frac{1}{2}\boldsymbol{s}_v^T \boldsymbol{s}_v + \frac{1}{2}\boldsymbol{s}_\psi^T \boldsymbol{s}_\psi}_{\text{observer}} + \underbrace{\frac{1}{2}M e_v^2 + \frac{1}{2}k_{iv} z_v^2}_{\text{speedtrack}}. \tag{A14}$$

The stability proof of observer has been proved, as shown in Appendix A. Therefore, the slow subsystem is stable if the speed track is stable

$$\begin{aligned} \dot{V}_{\text{speed}} = & -K_T k_{pv} e_v^2 - K_T k_{pv} e_v \tilde{\omega} - K_T k_{iv} e_v z_v \\ & + e_v F_L + k_{iv} z_v e_v \\ \leq & -\left(K_T k_{pv} \left(1 + \frac{1}{2\varepsilon_1} \right) + \frac{K_T k_{iv}}{2\varepsilon_2} + \frac{1}{2\varepsilon_3} + \frac{k_{iv}}{2\varepsilon_4} \right) e_v^2 \\ & - \frac{\varepsilon_1}{2} K_T k_{pv} \tilde{\omega}^2 - \left(\frac{\varepsilon_2}{2} K_T k_{iv} - \frac{\varepsilon_4}{2} \right) z_v^2 + \frac{\varepsilon_3}{2} F_L^2 \end{aligned} \tag{A15}$$

where ε_1, ε_2, ε_3, and ε_4 are positive constants.

According to the coefficients of current PI controller (A13), (A15) can be transformed into

$$\dot{V}_{\text{speed}} \leq -\kappa_1 e_v^2 - \kappa_2 z_v^2 - \kappa_3 \tilde{\omega}^2 + \frac{\varepsilon_3}{2} F_L^2. \tag{A16}$$

Since the load force is bounded, the derivative of Lyapunov function for slow subsystem can be derived from (A14) and (A16), as given by

$$\dot{V}_{\text{slow}} \leq -\kappa_4 V_{\text{slow}} + \kappa_5 \tag{A17}$$

where κ_4 and κ_5 are positive. It means that the slow subsystem is also stable.

This comprehensive stability proof provides theoretical justification for the excellent performance demonstrated by the FOTSM-based sensorless LIM control system in experimental results. The system maintains robust stability under parameter variations and external disturbances while ensuring smooth, chattering attenuation operation through the integral-type control laws.

C. Main Parameters of Motors A and B

TABLE II
MAIN PARAMETERS OF MOTOR A

Symbol	Name	Value and Unit
L_m	Mutual inductance	35 mH
L_{l1}	Primary leakage	9 mH
L_{l2}	Secondary leakage	3.8 mH
R_1	Primary resistance	1.06 Ω
R_2	Secondary resistance	2.4 Ω
v_{2N}	Rated speed	11 m/s
F_N	Rated thrust	270 N

TABLE III
MAIN PARAMETERS OF MOTOR B [28]

Symbol	Name	Value and Unit
L_m	Mutual inductance	26.477 mH
L_{l1}	Primary leakage	6.688 mH
L_{l2}	Secondary leakage	2.091 mH
R_1	Primary resistance	0.1382 Ω
R_2	Secondary resistance	0.576 Ω
v_{2N}	Rated speed	11 m/s
F_N	Rated thrust	10800 N

REFERENCES

[1] Y. Tang, W. Xu, D. Dong, Y. Liu, and M. M. Ismail, "Low-complexity multistep sequential model predictive current control for three-level inverter-fed linear induction machines," *IEEE Trans. Ind. Electron.*, vol. 70, no. 6, pp. 5537–5548, Jun. 2023.

[2] W. Xu et al., "Discrete space vector modulation-based MPCC with inductance identification for thrust ripple suppression in linear induction machine," *IEEE Trans. Power Electron.*, vol. 39, no. 10, pp. 12883–12893, Oct. 2024.

[3] R. Dian, W. Xu, J. Zhu, D. Hu, and Y. Liu, "An improved speed sensorless control strategy for linear induction machines based on extended state observer for linear metro drives," *IEEE Trans. Veh. Technol.*, vol. 67, no. 10, pp. 9198–9210, Oct. 2018.

[4] W. Xu, J. G. Zhu, Y. Zhang, Y. Li, Y. Wang, and Y. Guo, "An improved equivalent circuit model of a single-sided linear induction motor," *IEEE Trans. Veh. Technol.*, vol. 59, no. 5, pp. 2277–2289, Jun. 2010.

[5] T. Wang, B. Wang, Y. Yu, and D. Xu, "High-order sliding-mode observer with adaptive gain for sensorless induction motor drives in the wide-speed range," *IEEE Trans. Ind. Electron.*, vol. 70, no. 11, pp. 11055–11066, Nov. 2023.

[6] M. Zhou, S. Cheng, Y. Feng, W. Xu, L. Wang, and W. Cai, "Full-order terminal sliding-mode-based sensorless control of induction motor with gain adaptation," *IEEE J. Emerg. Sel. Top. Power Electron.*, vol. 10, no. 2, pp. 1978–1991, Apr. 2022.

[7] L. Zhang, H. Zhang, H. Obeid, and S. Laghrouche, "Time-varying state observer based twisting control of linear induction motor considering dynamic end effects with unknown load torque," *Instrum. Soc. Amer. Trans.*, vol. 93, pp. 290–301, Oct. 2019.

[8] L. Wogi, M. Morawiec, and T. Ayana, "Sensorless control of induction motor based on super-twisting sliding mode observer with speed convergence improvement," *IEEE Access*, vol. 12, pp. 74239–74250, 2024.

[9] W. Sun, D. Xu, Z. Liu, and Z. Wang, "The universality analysis of virtual voltage injection method for different observers in speed sensorless IM drives," *IEEE J. Emerg. Sel. Top. Power Electron.*, vol. 9, no. 3, pp. 2818–2838, Jun. 2021.

[10] Y.-D. Yoon and S.-K. Sul, "Sensorless control for induction machines based on square-wave voltage injection," *IEEE Trans. Power Electron.*, vol. 29, no. 7, pp. 3637–3645, Jul. 2014.

[11] W. Sun, Z. Wang, D. Xu, and B. Wang, "Robust stability improvement for speed sensorless induction motor drive at low speed range by virtual voltage injection," *IEEE Trans. Ind. Electron.*, vol. 67, no. 4, pp. 2642–2654, Apr. 2020.

[12] W. Sun, D. Xu, and D. Jiang, "Observability analysis for speed sensorless induction motor drives with and without virtual voltage injection," *IEEE Trans. Power Electron.*, vol. 34, no. 9, pp. 9236–9246, Sep. 2019.

[13] H. Wang, X. Ge, Y. Yue, and Y.-C. Liu, "Dual phase-locked loop based speed estimation scheme for sensorless vector control of linear induction motor drives," *IEEE Trans. Ind. Electron.*, vol. 67, no. 7, pp. 5900–5912, Jul. 2020.

[14] H. Wang, Y. Yang, X. Ge, S. Li, and Y. Zuo, "Speed-sensorless control of linear induction motor based on the SSLKF-PLL speed estimation scheme," *IEEE Trans. Ind. Appl.*, vol. 56, no. 5, pp. 4986–5002, Sep./Oct. 2020.

[15] L. Zhao, J. Huang, J. Chen, and M. Ye, "A parallel speed and rotor time constant identification scheme for indirect field oriented induction motor drives," *IEEE Trans. Power Electron.*, vol. 31, no. 9, pp. 6494–6503, Sep. 2016.

[16] H. Wang, Y.-C. Liu, and X. Ge, "Sliding-mode observer-based speed-sensorless vector control of linear induction motor with a parallel secondary resistance online identification," *Int. Eng. Technol. Elect. Power Appl.*, vol. 12, no. 8, pp. 1215–1224, Jan. 2019.
[17] A. Accetta, M. Cirrincione, M. Pucci, and G. Vitale, "Closed-loop MRAS speed observer for linear induction motor drives," *IEEE Trans. Ind. Appl.*, vol. 51, no. 3, pp. 2279–2290, May/Jun. 2015.
[18] B. Chen, W. Yao, F. Chen, and Z. Lu, "Parameter sensitivity in sensorless induction motor drives with the adaptive full-order observer," *IEEE Trans. Ind. Electron.*, vol. 62, no. 7, pp. 4307–4318, Jul. 2015.
[19] M. Cirrincione, A. Accetta, M. Pucci, and G. Vitale, "MRAS speed observer for high-performance linear induction motor drives based on linear neural networks," *IEEE Trans. Power Electron.*, vol. 28, no. 1, pp. 123–134, Jan. 2013.
[20] A. Accetta, M. Cirrincione, M. Pucci, and G. Vitale, "Neural sensorless control of linear induction motors by a full-order Luenberger observer considering the end effects," *IEEE Trans. Ind. Appl.*, vol. 50, no. 3, pp. 1891–1904, May/Jun. 2014.
[21] M. Morawiec and A. Lewicki, "Speed observer structure of induction machine based on sliding super-twisting and backstepping techniques," *IEEE Trans. Ind. Informat.*, vol. 17, no. 2, pp. 1122–1131, Feb. 2021.
[22] L. Zhao, J. Huang, H. Liu, B. Li, and W. Kong, "Second-order sliding-mode observer with online parameter identification for sensorless induction motor drives," *IEEE Trans. Ind. Electron.*, vol. 61, no. 10, pp. 5280–5289, Oct. 2014.
[23] H. Wang, X. Ge, and Y.-C. Liu, "Second-order sliding-mode MRAS observer-based sensorless vector control of linear induction motor drives for medium-low speed Maglev applications," *IEEE Trans. Ind. Electron.*, vol. 65, no. 12, pp. 9938–9952, Dec. 2018.
[24] D. Dong, W. Xu, X. Xiao, and Y. Liu, "Online magnetizing inductance identification strategy of linear induction motor based on second-order sliding-mode observer and MRAS," in *Proc. 13th Int. Symp. Linear Drives Ind. Appl.*, 2021, pp. 1–6.
[25] J. Duncan, "Linear induction motor-equivalent-circuit model," *Proc. Inst. Elect. Eng.*, vol. 130, no. 1, pp. 51–57, Jan. 1983.
[26] D. Dong, W. Xu, X. Xiao, Y. Tang, and K. Yang, "Online identification strategy of secondary time constant and magnetizing inductance for linear induction motors," *IEEE Trans. Power Electron.*, vol. 37, no. 10, pp. 12450–12462, Oct. 2022.
[27] I. Boldea, M. C. Paicu, and G.-D. Andreescu, "Active flux concept for motion-sensorless unified AC drives," *IEEE Trans. Power Electron.*, vol. 23, no. 5, pp. 2612–2618, Sep. 2008.
[28] T. Higuchi, S. Nonaka, and M. Ando, "On the design of high-efficiency linear induction motors for linear metro," *Elect. Eng. Jpn.*, vol. 137, no. 2, pp. 36–43, Aug. 2001.
[29] T. Song, M. F. Rahman, K. W. Lim, and M. A. Rahman, "A singular perturbation approach to sensorless control of a permanent magnet synchronous motor drive," *IEEE Trans. Energy Convers.*, vol. 14, no. 4, pp. 1359–1365, Dec. 1999.
[30] M. Ghanes and G. Zheng, "On sensorless induction motor drives: Sliding-mode observer and output feedback controller," *IEEE Trans. Ind. Electron.*, vol. 56, no. 9, pp. 3404–3413, Sep. 2009.

Siwei Cheng was born in Yancheng, China. He received the B.E. degree in building electrical and intelligent from Yangzhou University, Yangzhou, China, in 2019, and the M.E. degree in electrical engineering from Harbin University of Science and Technology, Harbin, China, in 2022. He is currently working toward the Ph.D. degree in electrical engineering at the State Key Laboratory of Advanced Electromagnetic Engineering and Technology, Huazhong University of Science and Technology, Wuhan, China.

His research interests include robust control and sensorless control for linear machine.

Wei Xu (Fellow, IEEE) received the double B.E. and M.E. degrees from Tianjin University, Tianjin, China, in 2002 and 2005, respectively, and the Ph.D. degree from the Institute of Electrical Engineering, Chinese Academy of Sciences (IEECAS), Beijing, China, in 2008, all in electrical engineering.

His research topics mainly focus on the design and control of linear machines and drives. From 2008 to 2012, he was a Post-Doctoral Fellow with the University of Technology Sydney, Ultimo, NSW, Australia, the Vice-Chancellor Research Fellow with the Royal Melbourne Institute of Technology, Melbourne, VIC, Australia, and a Japan Science Promotion Society Invitation Fellow with Meiji University, Tokyo, Japan, respectively. From 2013 to 2023, he was a Professor with the Huazhong University of Science and Technology, Wuhan, China. Since 2024, he has been a Professor with IEECAS and Director for State Key Laboratory.

Dr. Xu is a Fellow of the Institute of Engineering and Technology. He was the General Chair of 2021 International Symposium on Linear Drives for Industry Applications and 2023 IEEE International Conference on Predictive Control of Electrical Drives and Power Electronics. He is an Associate Editor of more than ten peer-reviewed IEEE JOURNALS, including IEEE TRANSACTIONS ON INDUSTRIAL ELECTRONICS and IEEE TRANSACTIONS ON POWER ELECTRONICS.

Jian Ge (Member, IEEE) was born in Heilongjiang, China, in 1994. He received the B.E., M.E., and Ph.D. degrees in electrical engineering from Huazhong University of Science and Technology, Wuhan, China, in 2016, 2019, and 2022, respectively.

From 2022 to 2025, he was a Postdoctoral Researcher in electrical engineering with Huazhong University of Science and Technology. He is currently an Assistant Research Fellow with the State Key Laboratory of High-Density Electrical Energy Conversion, Huazhong University of Science and Technology. His research interests include linear induction machines, high-power/torque-density electric machines and brushless doubly-fed machines.

Yirong Tang received the B.E. and Ph.D. degrees in electrical engineering from Huazhong University of Science and Technology, Wuhan, China, in 2020 and 2025, respectively.

He is currently a Postdoctoral Researcher in electrical engineering with the Institute of Electrical Engineering, Chinese Academy of Sciences, Beijing, China. His research interests include advanced control methods for linear induction machine drive system.

Han Xiao is currently working toward the Ph.D. degree in electrical engineering with Huazhong University of Science and Technology, Wuhan, China.

His research interests include model predictive control for linear induction machines and power converters.

Zhongyong Chen received the B.E. degree in physics from Shaanxi Normal University, Xi'an, China, in 2001, and the Ph.D. degree in plasma physics from the Institute of Plasma Physics, Chinese Academy of Sciences, Beijing, China, in 2006.

He was funded by the Fok Yingdong University Young Teacher Fund in 2008, selected into the first batch of talents of the ITER Special Program of the Ministry of Science and Technology in 2009, and engaged in plasma cracking research at the National Fusion Research Institute of Korea, from 2010 to 2011. He is currently a Professor and the Ph.D. Supervisor with the Huazhong University of Science and Technology, Wuhan, China, and he is an Expert of the International ITPA Topical Group on MHD, Disruptions and Control Committee.

Ion Boldea (Life Fellow, IEEE) received the M.S. and Ph.D. degrees in electrical engineering from the University Politehnica of Timisoara, Timisoara, Romania, in 1967 and 1973, respectively.

He is currently a Full Professor with the University Politehnica of Timisoara. His research interests include linear and rotary electric machines, drives, and MAGLEVs.

Dr. Boldea was the recipient of the 2015 IEEE Nikola Tesla Award.